Implementation of Active Damping Control Methodology on Modular Multilevel Converter(MMC)-Based Arbitrary Wave Shape Generator Used for High Voltage Testing

Xiaochuan Zhou[1], Dhanashree Ashok Ganeshpure[1], Thiago Batista Soeiro[3], Mohamad Ghaffarian Niasar[1], Yang Wu[1]and Peter Vaessen[1,2]

[1]DELFT UNIVERSITY OF TECHNOLOGY Delft, The Netherlands
[2]KEMA LABORATORIES Arnhem, The Netherlands
[3]UNIVERSITY OF TWENTE Twente, The Netherlands
E-Mail: X.Zhou-17@student.tudelft.nl

ACKNOWLEDGMENT

The work was carried out as part of HV-AWG project supported by Dutch TKI Urban Energy program which is greatly acknowledged.

***Index Terms*—Modular Multilevel Converters (MMC), Phase-Shift Mode, Active damping, Controllers PI control, Stability analysis**

***Abstract*—In order to damp the resonance in the MMC-based Arbitrary Wave shape Generator (AWG) used for high voltage testing, an active damping control methodology is proposed in this paper instead of the passive damping with an arm resistor. It is vital to ensure the system's stability when such an active damping closed loop control is implemented. Consequently, optimal parameters of a PI controller are designed by analyzing the stability margins of the involved transfer function using Bode-Plots. The performance of the designed active damping control methodology and the PI controller have been demonstrated with a $50\,\mathrm{Hz}$ sinusoidal waveform and arbitrary waveforms such as triangular, trapezoidal, and complex waveforms in MATLAB-Simulink. These results proves that the output voltage can track the reference without any reasonable error and does not contain any resonant frequency. Additionally, the Total Harmonic Distortion (THD) of the sinusoidal waveform and other arbitrary waveforms is less than 1% with the Phase Shift Carrier (PSC) modulation technique.**

I. INTRODUCTION

High Voltage (HV) equipment in the electrical power system, such as switchgear, cables, and transformers, are experiencing new electrical stresses due to the rise of Distribution Generation (DG) systems and large renewable energy integration by power electronic converters [1]- [2]. Since existing HV test sources have many limitations in generating arbitrary wave shapes, a Modular Multilevel Converter (MMC)-based Arbitrary Wave Shape Generator (AWG) is proposed in [2]. During an HV test of the equipment mentioned above, its equivalent electrical circuit is capacitive, as described in [2]. The arm inductor and the capacitive load create an LC resonant circuit, resulting in oscillation in the output voltage and current of the MMC-based AWG. It is important to attenuate the oscillations to avoid any unnecessary voltage stress applied to the test object and to obtain high-quality voltage waveforms. Typically, the resonance can be suppressed passively using an arm resistor or actively with a controll loop [3]. A common practice in conducting HV tests is to use a resistor to suppress oscillations [2]. Therefore, first, the performance of the MMC-based AWG is showcased in [2] with passive damping technique by means of an arm resistor. Although passive damping simplifies the control architecture and provides satisfactory results, it creates losses in the arm resistor as the DC link voltage increases. Furthermore, the resistance of the arm limits the maximum magnitude of the circulating current flowing through the circuit, limiting the voltage balancing capability of the submodule capacitor of the MMC. Therefore, this article investigates the active damping control methodology for the MMC-based AWG.

The active damping techniques have been extensively researched and developed based on the conventional three-phase, two-level, and three-level (NPC and T-type) topologies [4]- [8]. It can generally be categorized into filter-based [4]- [6] and loop-feedback-based methods [7]- [8]. The filter-based active damping is realized by cascading the designed filter, for instance, the notch filter in the current control loop. Loop-feedback-based

active damping measures the capacitor voltage or current and feedback to the controller output. This paper proposes the filter-based active damping methodology to attenuate resonance without adding a large lossy arm resistor. Active damping control has been implemented in MMC control to suppress unwanted high-frequency, as discussed in [9]- [11]. However, all the existing literature studies it for sinusoidal reference. This paper analyses and demonstrates it for different arbitrary wave shapes, such as triangular waveforms, trapezoidal waveforms, and superimposed waveforms. The filter implementation plays a critical role in obtaining high-quality voltage waveforms. Additionally, it is important to study the stability considering the two different control loops present. Hence, the main contribution of the paper is as follows:

1) Study the stability of the implemented closed loop control with active damping.
2) Illustrate the performance of MMC-based AWG when the active damping methodology is implemented with non-sinusoidal arbitrary wave shapes
3) Compare the performance of the active damping methodology with different modulation techniques such as Phase Shift Carrier (PSC) and Nearest Level Control (NLC).

In this paper, Section II describes the schematics of the MMC-based AWG and summarizes the specifications of the MMC-based AWG. Later, the control system is proposed, and the overall implementation of the active damping control circuit as well as the discrete-time equivalent control systems, are discussed in Section III. Additionally, according to the results of the stability margin analysis, the Bode plots with variable Kp and Ki are analyzed in Section IV. The MATLAB-Simulink simulations of the MMC-based AWG are discussed in Section V, where multiple arbitrary waveforms are generated. In the end, Section VI concludes the work with future recommendations.

II. Schematic and Specifications of the MMC-based HV AWG

Fig.1(a) shows the schematic of the MMC-based HV AWG, which has been adapted from the original MMC topology for the application of power transmission [2]. It has a single phase of an MMC, a split DC source, the AC filter comprising the arm inductance, arm resistor, and a capacitive load representing the equivalent electrical model of the HV equipment. Here, the split DC source is realized using the two DC link capacitors in series. The complex MMC circuit can be decoupled into two circuits as shown in Fig.1(b) and Fig. 1(c). The first circuit is the output current circuit where the inner emf (v_s) is filtered by the low pass filter (L_a, R_a and C_{load}) and accurate voltage waveforms are generated across the load capacitor. From this circuit, the expected resonance frequency can be calculated from $\omega_c = \sqrt{2/(L_a C_{load})}$. Additionally, the output current circuit determines the plant transfer function to be used to study the stability criteria of the implemented control Methodology and it is discussed in detail in the upcoming sections. The second circuit is the circulating current circuit which determines the dynamics involved in balancing submodule capacitor voltages. Also, it clearly shows the influence of the arm resistor directly on the magnitude of the circulating current.

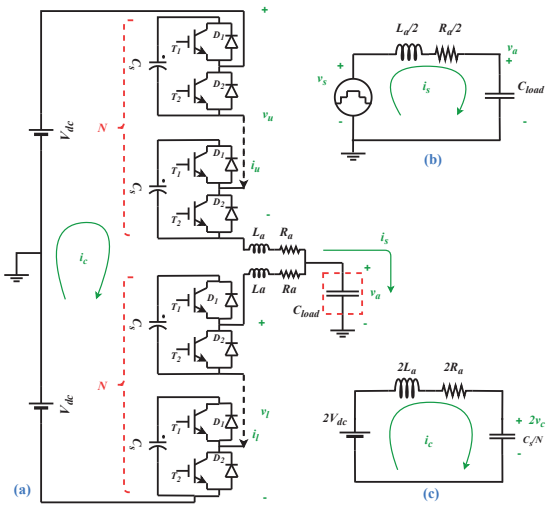

Fig. 1: Schematic of MMC-based HV AWG [2]

Among a wide variety of modulation techniques available for the MMC, one can clarify them into two categories defined by the operating switching frequency of the submodules: high-frequency and low-frequency modulations. The high-frequency modulation techniques are classified into Carrier-based or Space vector modulation techniques. Moreover, carrier-based modulation can be divided into Phase-Shifted Carrier (PSC) [12] and Level-Shifted Carrier (LSC) [13]. PSC is chosen over LSC or space vector modulation due to its inherent nature in balancing submodule capacitor voltages [14]. Low-frequency modulation can be divided into Selective Harmonic Elimination (SHE), Nearest Level Control (NLC), and Nearest Vector Control (NVC) [15]. Here, the NLC is chosen considering that the SHE becomes complicated if there are too many SMs and pulses to optimize in an HVDC system, while the NVC has a limited range of open-loop operations [16]- [17].

The MMC-based HV AWG is designed to generate a maximum output voltage of $100\,\mathrm{kV}$ for targeting Medium Voltage class equipment which ranges from $1\,\mathrm{kV}$ to $36\,\mathrm{kV}$ [2]. Note that the $36\,\mathrm{kV}$ need to be tested for a voltage higher than its rated voltage, such as $80\,\mathrm{kV}$ to $100\,\mathrm{kV}$ considering the switching transients that occur in the electric power network. Additionally, as explained above, these MV equipment behaves as a capacitance with a range of $50\,\mathrm{pF}$ and $10\,\mathrm{nF}$ to include all different types of HV components, such as switchgear, cables, and transformers [2]. In this article as the feasibility study of the proposed algorithm, the performance of the proposed active damping methodology is presented in a down-scaled MMC simulation, where the peak output voltage is scaled to $150\,\mathrm{V}$ from $100\,\mathrm{kV}$ and the capacitive load to $6.8\,\mu\mathrm{F}$ from $10\,\mathrm{nF}$ to keep the arm current flowing the same. Here, the number of submodules per arm is taken as 12. Additionally, the arm inductor is designed to be $1.32\,\mathrm{mH}$, and the value of the arm resistor is taken to be very small, as $10\,\Omega$. All these system specifications are summarized in Tab.I.

Tab. I. System Parameters of the MMC Setup

Description	Symbol	Values
DC-link voltage	2Vdc	300 V
Modulation index	mreq	0.8
Number of submodules	N	12
Switching frequency	Fs	3770 Hz
Frequency of input waveform	freq	50 Hz
Arm resistance	Ra	10 Ω
Arm inductance	La	1.32 mH
Load capacitance	Cload	6.8 μF

III. CONTROL SYSTEM DESIGN

A. Control system

Fig.2 shows the proposed closed-loop control configuration for the MMC-based AWG. The voltage feedback ensures the minimal steady-state error. The band pass filter measures the output current waveform to identify the resonance frequency in the MMC circuit. Considering the two control loops present in the proposed control configuration, it is important to study the stability of the proposed control system, as it will be shown in the upcoming sections.

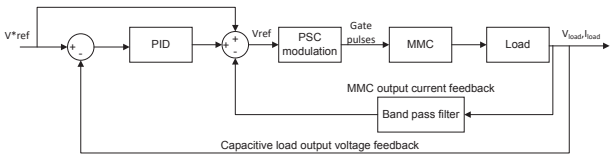

Fig. 2: Closed loop system of the MMC-based AWG

B. Design of control loop in continuous-time domain

The detailed block diagram of the control system in the continuous-time domain is shown in Fig.3. To study the stability of the closed-loop control, the transfer functions of each block are needed, such as the controller ($\mathrm{Gk(s)}$), the plant ($\mathrm{Gp(s)}$), the band pass filter ($\mathrm{Gb(s)}$), and the load ($\mathrm{Gload(s)}$) and they are derived in the following sections. Additionally, there are several system delays to consider in studying the stability of the control system. First, the computational delay represents the amount of time between the sampling instant and the duty cycle updating instant [18]. Second, the PCIe (Peripheral Component Interconnect Express) delay in the forward and feedback paths is present due to the architecture of the real-time simulator, where $\mathrm{T_s}$ is the simulation step of the real-time simulator.

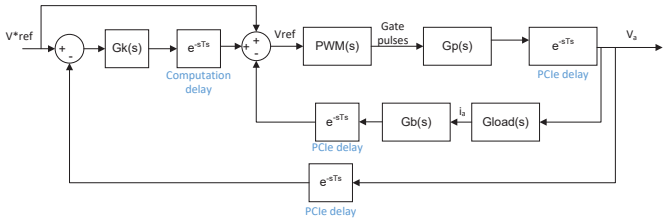

Fig. 3: Block diagram of the control system of the MMC-based AWG as a continuous equivalent

1) PI controller ($G_k(s)$): The Proportional-Integral (PI) controller is one of the most widely used controllers in all converter topologies due to its simplicity and effective performance. An ideal representation of the PI controller is defined as shown in (1).

$$G_k(s) = K_p(1 + K_i\frac{1}{s}) \tag{1}$$

Here, K_p corresponds to the proportional gain, and K_i represents the integral gain. Additionally, the controller computation delay must be included since it impacts the stability of the closed-loop system. The combined transfer is shown in (2).

$$G_k'(s) = K_p e^{-sTs}(1 + K_i\frac{1}{s}) \tag{2}$$

2) Plant ($G_p(s)$): The output current circuit shown in Fig.1(b) dictates the dynamics of the MMC. Hence, the plant transfer function is derived from it in the following equations, where $V_a(s)$ and $V_s(s)$ are variables representing the output voltage and the switching voltage in the Laplace domain.

$$V_s(s) = s\frac{L_a}{2}I(s) + \frac{R_a}{2}I(s) + \frac{1}{s}\frac{I(s)}{C_{load}} \tag{3}$$

$$V_a(s) = \frac{1}{s}\frac{I(s)}{C_{load}} \tag{4}$$

$$G_p(s) = \frac{V_a(s)}{V_s(s)} = \frac{2}{s^2 L_a C_{load} + sR_a C_{load} + 2} \tag{5}$$

The transfer function representing the PWM process is shown in (6) [19]. An equivalent transfer function could be represented by a sampler with a gain of $1/\mathrm{Ts}$, followed by a zero order hold (ZOH) that compares the sampled input data with the carrier wave input data. m_{PWM} represents the ratio of the modulation amplitude to the carrier amplitude. Furthermore, (7) shows the combined transfer function for the plant in the forward path.

$$G_{PWM}(s) = \frac{m_{PWM}G_{zoh}(s)}{T_s} = \frac{m_{PWM}(1 - e^{-sT_s})}{sT_s} \tag{6}$$

$$G_p^{'}(s) = G_p(s)G_{PWM}(s)e^{-sTs} \tag{7}$$

3) Band pass filter ($Gb(s)$): As mentioned in the introduction, a filter-based active damping controller is proposed to suppress the resonance present in the MMC-based AWG. To do so, it is important to identify the resonant frequency in the output characteristics of the MMC-based HV AWG, and the band pass filter is selected by choosing particular band frequencies around the resonance (ωc) [11]. The filter operates between frequencies $\omega 1$ and $\omega 2$, and its transfer function is derived based on a typical RLC band pass filter. The physical implementation of such a series band pass filter is shown in Fig.4 [21], and its transfer function is derived from (8). Depending on the resonant frequency, the band pass filter can be altered by changing the values of $\omega 1$ and $\omega 2$.

$$\begin{aligned} G_b(s) &= \frac{R}{\frac{1}{sC} + sL + R} \\ &= \frac{s(\omega_2 - \omega_1)}{s^2 + s(\omega_2 - \omega_1) + \omega_1\omega_2} \end{aligned} \tag{8}$$

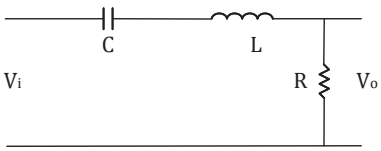

Fig. 4: Series band pass filter

where $\omega_1 = -\frac{1}{2RC} + \sqrt{\frac{1}{2R^2C^2} + \frac{1}{LC}}$ and $\omega_2 = \frac{1}{2RC} + \sqrt{\frac{1}{2R^2C^2} + \frac{1}{LC}}$.

In this control system, the resonance is measured from the output current. Therefore, the output current is obtained from the output voltage considering the capacitive load. On the basis of this relationship, the transfer of the band-pass filter is altered, including the PCIe delay, as shown in (10).

$$G_{load}(s) = \frac{I_a(s)}{V_a(s)} = sC \tag{9}$$

$$G_b^{'}(s) = \frac{G_b(s)}{sC}G_{load}(s)e^{-sTs} \tag{10}$$

C. Discretization of the closed-control loop

As the real-time simulator works with a fixed time step, studying the stability of the control implemented in the continuous domain may not provide an exact answer to the question. It is necessary to discretize the transfer functions from (2), (7), and (10).

The discretization of the PI controller in (2) is shown in (11) by placing $1/s = z/(z-1)$ for the integral gain and $e^{-sTs} = 1/z$.

$$G_k^{'}(z) = Z\left\{G_k^{'}(s)\right\} = \frac{k_p}{z}(1 + k_i\frac{z}{z-1}) \tag{11}$$

For plant discretization, the modulation index in the PWM transfer function is assumed to be 1 to simplify the process ($m_{PWM} = 1$). It should be noted that $G_{pwm}(s)$ need to be multiplied by T_s to compensate the $1/T_s$ in (6). Combining the plant transfer function and converting it into the z domain results in a discrete plant transfer function, as shown in (12).

$$
\begin{aligned}
G_p^{'}(z) &= Z\left\{G_p^{'}(s)\right\} \\
&= Z\left\{G_{pwm}(s)T_sG_p(s)e^{-sTs}\right\} \\
&= Z\left\{\frac{1-e^{-sT_s}}{sT_s}T_sG_p(s)e^{-sTs}\right\} \\
&= \frac{z(-(1+B)e^{-YT_s}-(1+C)e^{-XT_s}-B-C)}{(z-e^{-XT_s})(z-e^{-YT_s})} \\
&+ \frac{(e^{-XT_s-YT_s}+Be^{-YT_s}+Ce^{-XT_s})}{(z-e^{-XT_s})(z-e^{-YT_s})} \\
B &= \frac{Y}{X-Y}; C = \frac{X}{Y-X} \\
X &= \frac{R_aC_{load}+\sqrt{R_a^2C_{load}^2-8L_aC_{load}}}{2L_aC_{load}} \\
Y &= \frac{R_aC_{load}-\sqrt{R_a^2C_{load}^2-8L_aC_{load}}}{2L_aC_{load}}
\end{aligned}
\tag{12}
$$

Similarly, the band-pass filter is converted from the Laplace domain to the Z domain.

$$
\begin{aligned}
G_b{}'(z) &= Z\left\{G_b^{'}(s)\right\} \\
&= \frac{N^2(e^{2M-N}-e^{-N})}{M(ze^{2M-N})-z^2e^M-e^{M-2N}+ze^{-N})} \\
&+ \frac{N(e^{2M-N}-2ze^M+e^{-N})}{(ze^{2M-N})-z^2e^M-e^{M-2N}+ze^{-N})} \\
M &= \frac{\sqrt{\omega_1^2-6\omega_1\omega_2+\omega_2^2}}{2}; N = \frac{\omega_2-\omega_1}{2}
\end{aligned}
\tag{13}
$$

Therefore, the whole discretization system can be simplified and represented as shown in the block diagram in Fig.5.

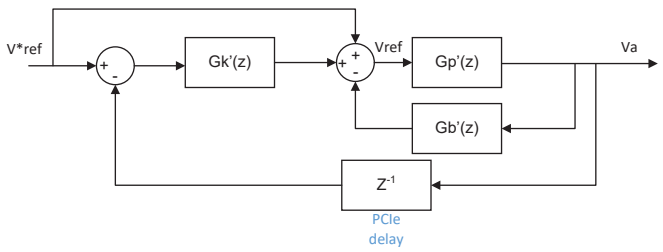

Fig. 5: Simplified discretization system

IV. Discussion of the stability analysis

To ensure the safe operation of the hardware, it is essential to analyze the stability of the system. The stability criteria is studied with the gain margin and phase margin of an open-loop transfer function, and it is derived in (14). In addition, the closed-loop transfer function of the system is derived in (15).

$$
\begin{aligned}
G_{pFB}^{'}(z) &= \frac{G_p^{'}(z)}{G_p^{'}(z)G_b^{'}(z)+1} \\
G_{ol}(z) &= (1+G_k^{'}(z))G_{pFB}^{'}(z)
\end{aligned}
\tag{14}
$$

$$
G_{cl}(z) = (1+G_k^{'}(z))\frac{G_{pFB}^{'}(z)}{G_{pFB}^{'}(z)G_k^{'}(z)z^{-1}+1} \tag{15}
$$

As discussed in Section II, the load capacitance and the arm inductance are chosen to be $6.8\,\mu\mathrm{F}$ and $1.32\,\mathrm{mH}$, respectively. Thus, the expected resonant frequency is:

$$
\omega_c = \frac{1}{\sqrt{\frac{L_a}{2}C_{load}}} = 14\,927\,\mathrm{rad\,s^{-1}} = 2375\,\mathrm{Hz} \tag{16}
$$

Hence, the band pass filter is designed based on (10), where $\omega 1 = 14\,327\,\mathrm{rad\,s^{-1}}$ and $\omega 2 = 15\,527\,\mathrm{rad\,s^{-1}}$ are chosen to ensure that the bandwidth is wide enough. For a PI controller, the transient response of the regulation system is mostly determined by the proportional term, while the integral term impacts the steady-state response. Therefore, the two can be analyzed separately. Bode plots based on open-loop system transfer functions are shown in Fig.6 to Fig.7.

Fig.6 to Fig.7 illustrates some common observations. On the one hand, when Kp increases, the magnitude of the PI controller increases. On the other hand, a lower Kp keeps the system stable, but might provide a poor transient response to the system. The influence of Ki values on the stability is significantly less compared to Kp. Hence, the bode plot of much higher values of Ki are plotted in Fig. 7. Additionally, sample time affects delays in the discrete-time domain. After analyzing the influence of Kp and Ki, the PI controller is built with Kp = 0.001 and Ki = 0.01, since it offers a safe gain margin of 10.9 dB and a phase margin of 27.8 deg. The pzmap of the closed-loop system is drawn in Fig.8. According to the Jury stability criterion [20], the closed-loop system is stable.

V. Simulation results

The discussed analysis of the proposed active damping control methodology is demonstrated using MATLAB-Simulink simulations of MMC-based AWG

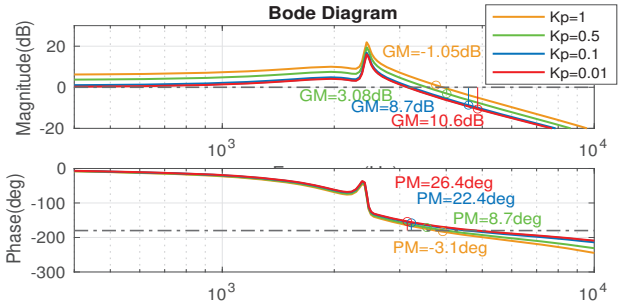

Fig. 6: Discrete domain: Variable Kp (Ki=0)

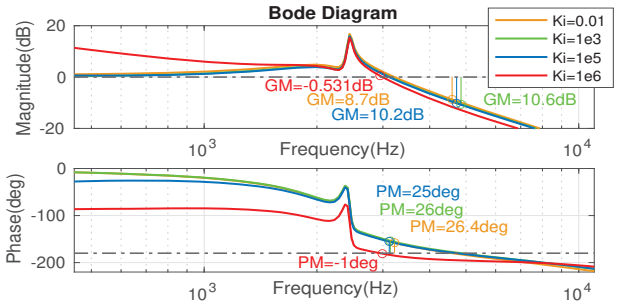

Fig. 7: Discrete domain: Variable Ki (Kp=0.01)

with 12 submodules per arm. As discussed earlier, the performance of two chosen modulation methods, PSC and NLC, is first compared in Fig.9. This figure shows that the PSC offers more accurate tracking of the reference voltage in the time domain and generates fewer base band harmonics in the frequency domain. It is observed that there is a significant difference in the quality of the waveforms obtained. Although PSC modulation can accurately track the reference voltage, NLC modulation

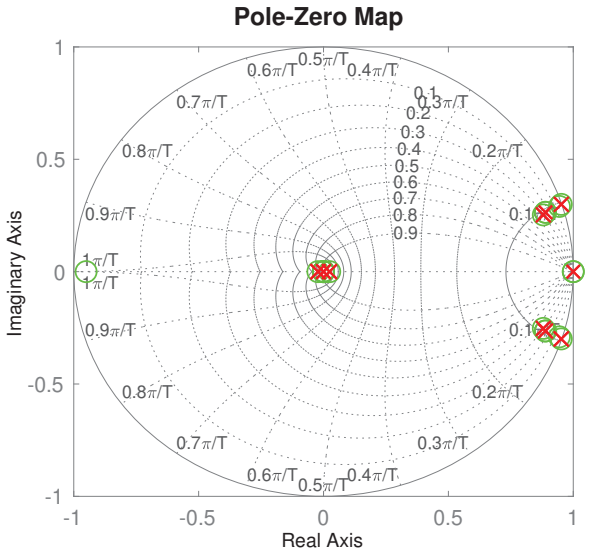

Fig. 8: Poles-zeros map with active damping

results in distortion, leading to a gap between the output voltage and the reference. This inaccuracy with NLC is due to the switching frequency being lower than that of PSC. This makes it difficult for the controller to correct the error. Therefore, the PSC modulation is chosen to generate the rest of the arbitrary voltage waveforms.

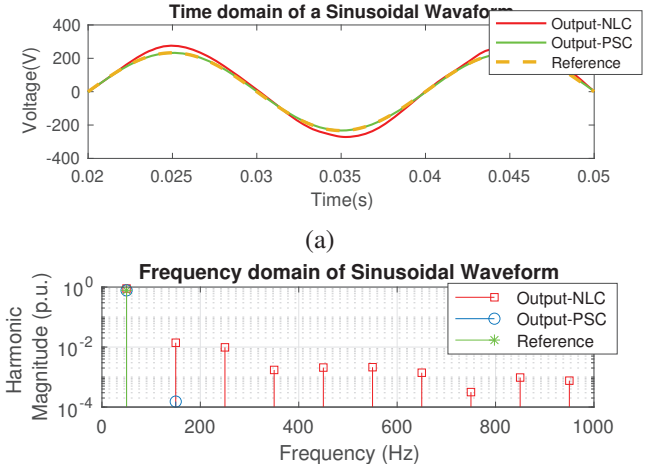

Fig. 9: Comparison between NLC and PSC with active damping control (a): Time domain (b) Frequency domain

Fig.10 illustrates the output results with active damping in both the time and frequency domains. As can be seen from Fig.10a, the output voltage significantly tracks the reference signals when active damping is applied, whereas without active damping, the output voltage has distortion, demonstrating that the proposed active damping method is effective. Additionally, the frequency domain analysis is conducted on the output voltage waveforms and reference waveforms, which shows that the generated output voltage waveforms match well with the reference waveform. Fig.10j illustrates that the sixth harmonic is a higher frequency spectrum since the complex waveform is compensated for by 10Hz sinusoidal and 50Hz trapezoidal waveforms.

Furthermore, the quality of the obtained waveforms is analyzed with the Total Harmonic Distortion (THD), and its definition is adapted for the non-sinusoidal voltage waveforms, as shown in (17) [2]. The obtained THD of the waveforms is less than 1 % summarized in Tab.II.

$$THD_{nonsin} = \frac{\sqrt{\sum_{h=0}^{\infty}(V_{h,ref} - V_{h,out})^2}}{V_{1,out}} \quad (17)$$

Tab. II. THD of MMC-Based AWG with PSC for Periodic Waveforms

Waveforms	THD(%)
Sinusoidal	0.02
triangular	0.194
Asymmetric triangular	0.645
Trapezoidal	0.264
Complex	0.500

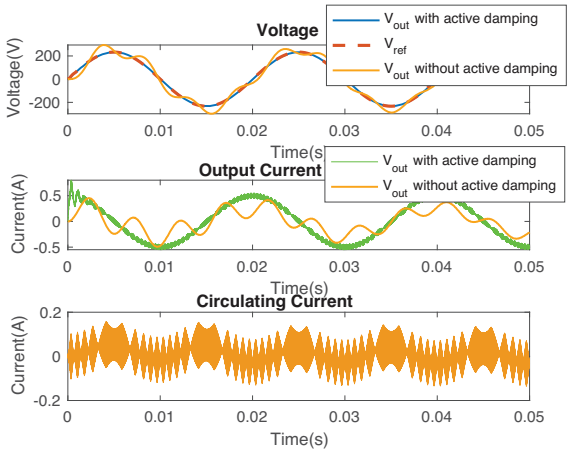

(a)

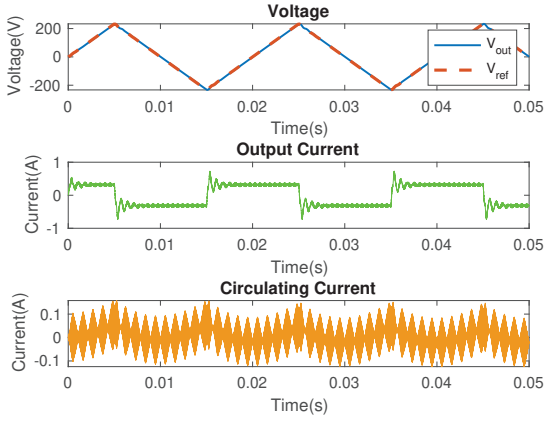

(b)

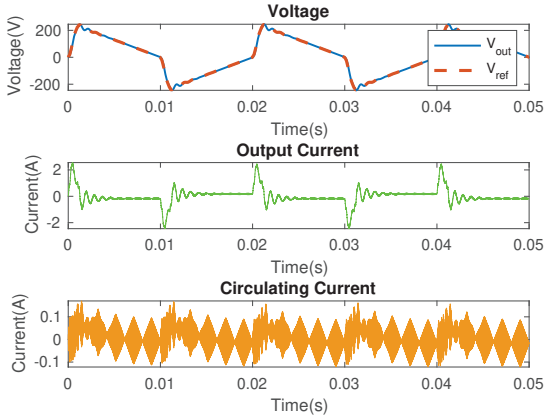

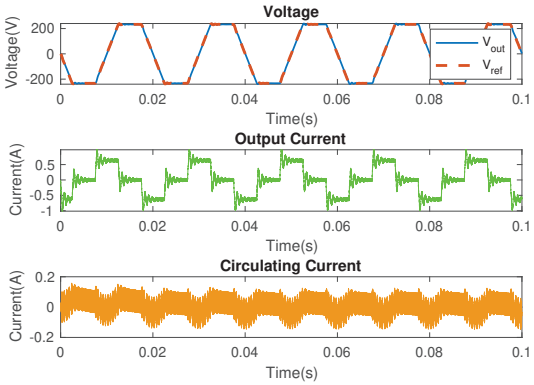

(d)

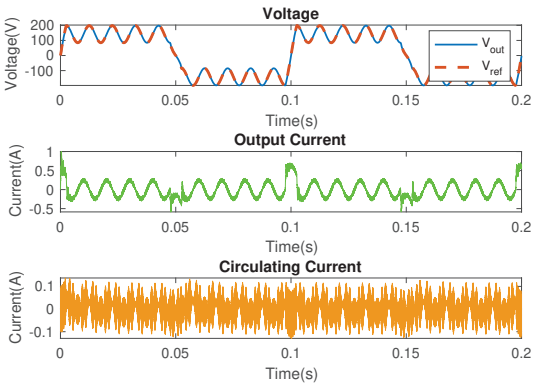

(e)

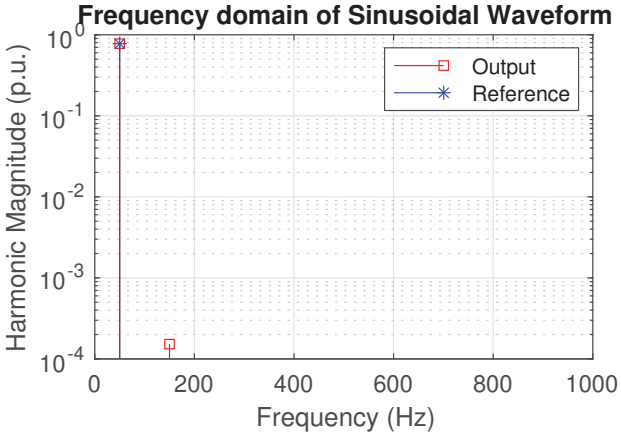

(f)

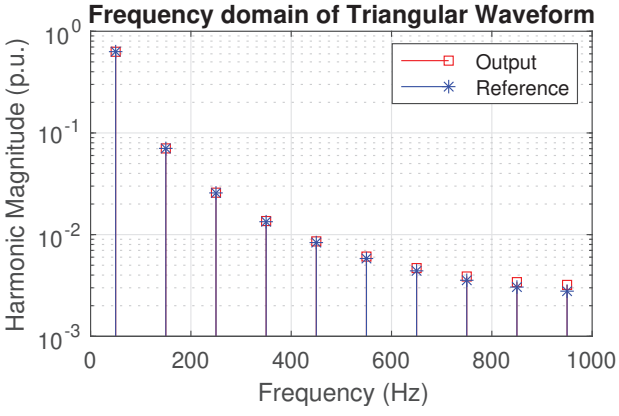

(g)

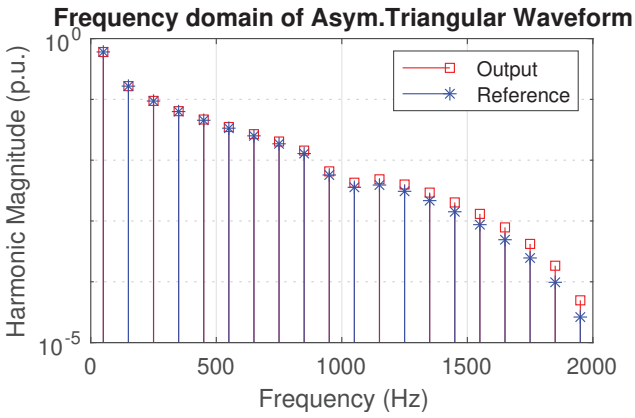

(h)

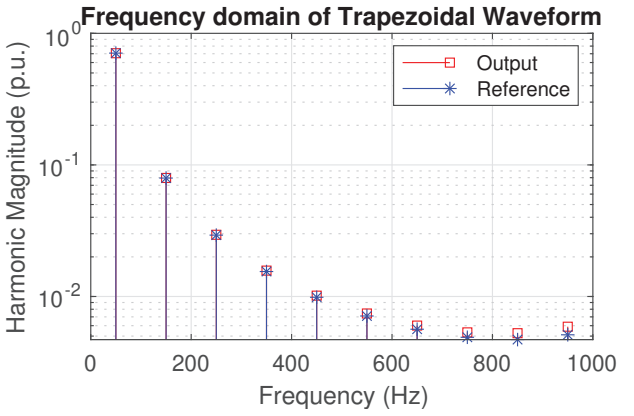

(i)

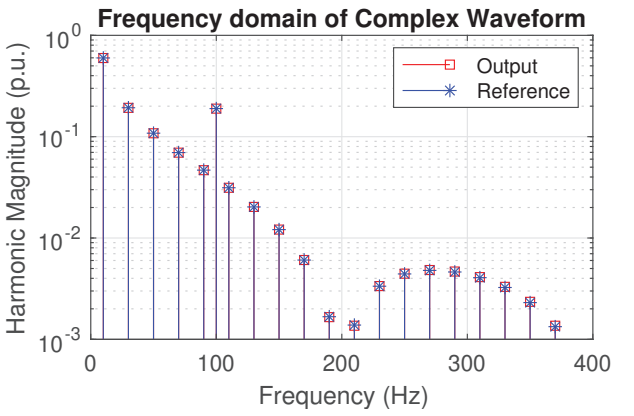

(j)

Fig. 10: Periodic waveforms generated from the MMC-based AWG (a) 50 Hz Sinusoidal time domain; (b) 50 Hz Triangular time domain; (c) 50 Hz Asymmetrical Triangular time domain; (d) 50 Hz Trapezoidal time domain; (e) Complex Waveform time domain; (f) Sinusoidal frequency domain; (g) Triangular frequency domain; (h) Asymmetrical Triangular frequency domain; (i) Trapezoidal frequency domain; (j) Complex Waveform frequency domain;

VI. Conclusion

This paper proposes and implements an active damping methodology for MMC-based AWG to suppress the oscillations in the converter. A bandpass filter is designed to measure the resonance generated between arm inductance and capacitive load. Additionally, the stability analysis is performed for the control system in the discrete domain, and the PI controller is tuned for the given desired MMC-based AWG parameter. The performance of the implemented active damping methodology is shown with the MATLAB-Simulink MMC model with 12 submodules per arm. The simulation results suggest that the PSC modulation technique generates more accurate waveforms with high switching frequency. Therefore, various waveforms such as triangular, trapezoidal, and a combination of trapezoidal and sinusoidal waveforms are generated from the MMC-based AWG with THD less than 1 %.

References

[1] T. Bengtsson et al., "Repetitive fast voltage stresses-causes and effects," *in IEEE Electrical Insulation Magazine*, vol. 25, no. 4, pp. 26-39, July-Aug. 2009.

[2] D. Ganeshpure, T. Batista Soeiro, M. G. Niasar, P. Vaessen, and P. Bauer, "Design trade-offs of modular multilevel converter-based arbitrary wave shape generator for conventional and unconventional high voltage testing," *IEEE Open Journal of the Industrial Electronics Society*, vol. 2, pp. 584–605, 2021.

[3] K. Ji, H. Pang, Z. He, Y. Li, D. Liu and G. Tang, "Active/Passive Method-Based Hybrid High-Frequency Damping Design for MMCs," *in IEEE Journal of Emerging and Selected Topics in Power Electronics*, vol. 9, no. 5, pp. 6086-6098, Oct. 2021, doi: 10.1109/JESTPE.2020.3044561.

[4] J. Dannehl, M. Liserre, and F. W. Fuchs, "Filter-based active damping of voltage source converters with lcl filter," *IEEE Transactions on Industrial Electronics*, vol. 58, no. 8, pp. 3623–3633, Aug 2011.

[5] W. Yao, Y. Yang, X. Zhang, F. Blaabjerg, and P. C. Loh, "Design and analysis of robust active damping for lcl filters using digital notch filters," *IEEE Transactions on Power Electronics*, vol. 32, no. 3, pp. 2360–2375, March 2017.

[6] S. Leitner, M. Yazdanian, S. Ziaeinejad, A. Mehrizi-Sani, and A. Muetze, "Internal model-based active resonance damping current control of a grid-connected voltage-sourced converter with an lcl filter," *IEEE Transactions on Power Systems*, vol. 33, no. 6, pp. 6025–6036, Nov 2018.

[7] D. Pan, X. Ruan, C. Bao, W. Li, and X. Wang, "Capacitor-currentfeedback active damping with reduced computation delay for improving robustness of lcl-type grid-connected inverter," *IEEE Transactions on Power Electronics*, vol. 29, no. 7, pp. 3414–3427, July 2014.

[8] . X. Wang, F. Blaabjerg, and P. C. Loh, "Virtual rc damping of lclfiltered voltage source converters with extended selective harmonic compensation," *IEEE Transactions on Power Electronics*, vol. 30, 10 2014.

[9] Y. Wu, A. Shekhar, T. B. Soeiro and P. Bauer, "Voltage Source Converter Control under Distorted Grid Voltage for Hybrid AC-DC Distribution Links," *IECON 2019 - 45th Annual Conference of the IEEE Industrial Electronics Society*, Lisbon, Portugal, 2019, pp. 5694-5699.

[10] T. Xia, Y. Huang, F. Peng, Y. Yao and Z. Cao, "Active damping control of modular multilevel converter with output filter for high-speed PM motor drive," *IECON 2017 - 43rd Annual Conference of the IEEE Industrial Electronics Society*, Beijing, China, 2017, pp. 1777-1782, doi: 10.1109/IECON.2017.8216301.

[11] Y. Li, H. Pang, M. Kong, J. Lu, K. Ji and G. Tang, "Compensation control and parameters design for high frequency resonance suppression of MMC-HVDC system," *in CSEE Journal of Power and Energy Systems*, vol. 7, no. 6, pp. 1161-1175, Nov. 2021.

[12] K. Ilves, L. Harnefors, S. Norrga and H. -P. Nee, "Analysis and operation of modular multilevel converters with phase-shifted carrier PWM," *2013 IEEE Energy Conversion Congress and Exposition*, Denver, CO, USA, 2013, pp. 396-403, doi: 10.1109/ECCE.2013.6646728.

[13] A. Hassanpoor, S. Norrga, H. -P. Nee and L. Ängquist, "Evaluation of different carrier-based PWM methods for modular multilevel converters for HVDC application," *IECON 2012 - 38th Annual Conference on IEEE Industrial Electronics Society*, Montreal, QC, Canada, 2012, pp. 388-393.

[14] W. van der Merwe, P. Hokayem and L. Stepanova, "Analysis of the N -Cell Single Phase MMC Natural Balancing Mechanism," *in IEEE Journal of Emerging and Selected Topics in Power Electronics*, vol. 2, no. 4, pp. 1149-1158, Dec. 2014.

[15] R. B. Jonnala, N. R. Eluri and S. B. Choppavarapu, "Implementation, comparison and experimental verification of nearest vector control and nearest level control techniques for 27-level asymmetrical CHB multilevel inverter," *2016 International Conference on Control, Instrumentation, Communication and Computational Technologies (ICCICCT)*, Kumaracoil, India, 2016, pp. 214-221.

[16] A. Dekka, B. Wu, N. R. Zargari and R. L. Fuentes, "A Space-Vector PWM-Based Voltage-Balancing Approach With Reduced Current Sensors for Modular Multilevel Converter," *in IEEE Transactions on Industrial Electronics*, vol. 63, no. 5, pp. 2734-2745, May 2016.

[17] R. B. Jonnala, N. R. Eluri and S. B. Choppavarapu, "Implementation, comparison and experimental verification of nearest vector control and nearest level control techniques for 27-level asymmetrical CHB multilevel inverter," *2016 International Conference on Control, Instrumentation, Communication and Computational Technologies (ICCICCT)*, Kumaracoil, India, 2016, pp. 214-221.

[18] J. Ma, X. Wang, F. Blaabjerg, L. Harnefors and W. Song, "Accuracy Analysis of the Zero-Order Hold Model for Digital Pulse Width Modulation," *in IEEE Transactions on Power Electronics*, vol. 33, no. 12, pp. 10826-10834, Dec. 2018.

[19] Y. Wu, T. B. Soeiro, A. Shekhar, J. Xu and P. Bauer, "Virtual Resistor Active Damping with Selective Harmonics Control of LCL-Filtered VSCs," *2021 IEEE 19th International Power Electronics and Motion Control Conference (PEMC)*, Gliwice, Poland, 2021, pp. 207-214.

[20] Jury, E. I.,"A Simplified Stability Criterion for Linear Discrete Systems," *Proceedings of the IRE*, vol. 50, no. 6, pp. 1493-1500, June 1962, doi: 10.1109/JRPROC.1962.288193.

[21] Tran, M., Anna Kuwana, and Haruo Kobayashi. "Design of Active Inductor and Stability Test for Passive RLC Low Pass Filter." 10th Int. Conf. on CCSEA. Vol. 10. No. 10. 2020.